

Article

Garnet-Type Zinc Hexacyanoferrates as Lithium, Sodium, and Potassium Solid Electrolytes

Leonhard Karger ¹, Saravanakumar Murugan ¹, Liping Wang ², Zhirong Zhao-Karger ^{3,4} , Aleksandr Kondrakov ^{1,5,*}, Florian Strauss ¹ and Torsten Brezesinski ^{1,*} 

- ¹ Battery and Electrochemistry Laboratory (BELLA), Institute of Nanotechnology, Karlsruhe Institute of Technology (KIT), Kaiserstr. 12, 76131 Karlsruhe, Germany; florian.strauss@kit.edu (F.S.)
² Institute for Organic Chemistry II and Advanced Materials, Ulm University, Albert-Einstein-Allee, 89081 Ulm, Germany; liping.wang@partner.kit.edu
³ Helmholtz Institute Ulm (HIU) Electrochemical Energy Storage, Helmholtzstr. 11, 89081 Ulm, Germany; zhirong.zhao-karger@kit.edu
⁴ Institute of Nanotechnology, Karlsruhe Institute of Technology (KIT), Kaiserstr. 12, 76131 Karlsruhe, Germany
⁵ BASF SE, Carl-Bosch-Str. 38, 67056 Ludwigshafen, Germany
* Correspondence: aleksandr.kondrakov@basf.de (A.K.); torsten.brezesinski@kit.edu (T.B.)

Abstract: Sodium-ion batteries offer an attractive alternative to lithium-based chemistries due to the lower cost and abundance of sodium compared to lithium. Using solid electrolytes instead of liquid ones in such batteries may help improve safety and energy density, but they need to combine easy processing with high stability toward the electrodes. Herein, we describe a new class of solid electrolytes that are accessible by room-temperature, aqueous synthesis. The materials exhibit a garnet-type zinc hexacyanoferrate framework with large diffusion channels for alkaline ions. Specifically, they show superionic behavior and allow for facile processing into pellets. We compare the structure, stability, and transport properties of lithium-, sodium-, and potassium-containing zinc hexacyanoferrates and find that $\text{Na}_2\text{Zn}_3[\text{Fe}(\text{CN})_6]_2$ achieves the highest ionic conductivity of up to 0.21 mS/cm at room temperature. In addition, the electrochemical performance and stability of the latter solid electrolyte are examined in solid-state sodium-ion batteries.



Citation: Karger, L.; Murugan, S.; Wang, L.; Zhao-Karger, Z.; Kondrakov, A.; Strauss, F.; Brezesinski, T. Garnet-Type Zinc Hexacyanoferrates as Lithium, Sodium, and Potassium Solid Electrolytes. *Batteries* **2024**, *10*, 365. <https://doi.org/10.3390/batteries10100365>

Academic Editor: Johan E. ten Elshof

Received: 16 September 2024

Revised: 8 October 2024

Accepted: 9 October 2024

Published: 16 October 2024



Copyright: © 2024 by the authors. Licensee MDPI, Basel, Switzerland. This article is an open access article distributed under the terms and conditions of the Creative Commons Attribution (CC BY) license (<https://creativecommons.org/licenses/by/4.0/>).

1. Introduction

As a complementary technology to lithium, solid-state sodium-ion batteries have emerged as a promising contender [1,2]. While it is important to note that they may not necessarily outperform conventional batteries in all aspects, they offer a compelling alternative with a focus on sustainability and an abundance of sodium resources. For this technology, the development of high-performance solid electrolytes is a key challenge, with different chemical approaches to enable sodium conduction in solids being reported in the literature [2].

Polymer electrolytes typically exhibit a low ionic conductivity at room temperature [3–5], which however can be enhanced by the addition of inorganic nanoparticles [6]. Superionic inorganic conductors can be considered an alternative to polymer electrolytes. Here, one has to differentiate between electrolytes of high- and low-temperature processability. Oxide-based electrolytes, such as sodium-beta alumina, $\text{Na}_3\text{Zr}_2\text{Si}_2\text{PO}_{12}$, or $\text{Na}_2\text{Zn}_2\text{TeO}_6$, are characterized by good stability against sodium (alloy) anodes and exhibit reasonably high ionic conductivities of up to ~0.7 mS/cm, but necessitate sintering into a thin (brittle) pellet, making commercialization efforts more challenging [7–10]. Halide electrolytes, such as $\text{Na}_{3-x}\text{Y}_{1-x}\text{Zr}_x\text{Cl}_6$, are more malleable and can be processed at low temperatures by cold pressing, but rely on costly and relatively scarce metal species and show only relatively low ionic conductivities [11–13]. Thiophosphate electrolytes derived from Na_3PS_4 are

among the most promising candidates, since they combine low-temperature processability with high ionic conductivity ($\sigma_{ion,rt} \leq 8.8 \text{ mS/cm}$), for example, if the material is modified with tungsten [14–16]. The main drawbacks of sulfide solid electrolytes are their limited stability in contact with the electrode active materials and susceptibility toward ambient atmosphere, the latter resulting in the release of toxic H_2S [17].

Recently, sodium conduction in Prussian blue analogues (PBAs), well-known cathode active materials (CAMs) for sodium-ion batteries, has been reported [18]. This material class combines the advantages of easy and scalable synthesis using low-cost precursors, stability at ambient conditions, and good processability (cold pressing), although their ionic conductivity is only comparable to that of halide electrolytes (up to $\sim 0.1 \text{ mS/cm}$) [18]. PBAs belong to a more general class of materials having the formula $X_a\text{TM}_b[\text{Fe}(\text{CN})_6]_c$, with X and TM being alkaline/alkaline-earth and transition-metal ions, respectively, and with the octahedral hexacyanoferrate $\text{Fe}(\text{CN})_6^{3-}$ [or $\text{Fe}(\text{CN})_6^{4-}$] as the basic building unit. This unit forms coordination polymers with a wide range of TM species. Depending on the coordination geometry of the TM by CN^- , different 3D structures are formed.

Herein, we introduce Zn^{2+} , leading to a shift from octahedral to tetrahedral coordination of the TM. This yields garnet-type zinc hexacyanoferrates of type $X_a\text{Zn}_3[\text{Fe}(\text{CN})_6]_2$ (ZHF) crystallizing in the space group $R-3c$, in which typical mobile X species are sodium and potassium ions. The open pore structure of ZHFs, combined with their stability in water and organic solvents, makes them interesting functional materials for a variety of applications, such as radioactive $^{137}\text{Cs}^+$ or $^{90}\text{Sr}^{2+}$ capture [19,20], photocatalysis [21], as ion-selective electrodes [22], or as CAMs for sodium- and potassium-ion batteries [23–26]. As cathodes, they exhibit lower theoretical and practical specific capacities than PBAs [27,28], but often show good performance at high current rates [23,25]. Similarly, in radioactive ion adsorption, K-ZHF shows much faster $^{137}\text{Cs}^+$ uptake than the related cubic $\text{Zn}_2[\text{Fe}(\text{CN})_6]$, indicating higher mobility in the garnet-type structure. This was an impetus for us to explore the ion mobility in various ZHFs, and examine their potential as solid electrolytes for rechargeable alkali-metal-ion batteries. We found the highest conductivity for sodium ions, which enabled us to demonstrate prototype solid-state sodium-ion batteries. Moreover, the ZHF materials outperform previously reported PBA cyanide frameworks in terms of room-temperature ionic conductivity.

2. Materials and Methods

Synthesis of $\text{Na}_2\text{Zn}_3[\text{Fe}(\text{CN})_6]_2$: In a round bottom flask, 5 g of $\text{Na}_4[\text{Fe}(\text{CN})_6]\cdot 10\text{H}_2\text{O}$ (1 eq.) and 6 g of NaCl (10 eq.) were dissolved in 200 mL of DI water. In a beaker, 2.76 g of $\text{ZnNO}_3\cdot 6\text{H}_2\text{O}$ (0.9 eq.) was dissolved in 100 mL of DI water. The zinc nitrate solution was added dropwise to the first solution under vigorous stirring at room temperature over a period of 30 min. The suspension was stirred for another 10 h and then left for sedimentation of the precipitate. The supernatant was removed, and the obtained white powder was washed three times using DI water with a 1:5 wt. ratio of powder to water. Subsequently, the material was dried overnight at the desired temperature, preferably at 90°C , under a dynamic vacuum.

Synthesis of $\text{K}_2\text{Zn}_3[\text{Fe}(\text{CN})_6]_2$: In a round bottom flask, 5 g of $\text{K}_4[\text{Fe}(\text{CN})_6]\cdot 10\text{H}_2\text{O}$ (1 eq.) and 6 g of KCl (10 eq.) were dissolved in 200 mL of DI water. In a beaker, 2.76 g of $\text{ZnNO}_3\cdot 6\text{H}_2\text{O}$ (0.9 eq.) was dissolved in 100 mL of DI water. The zinc nitrate solution was added dropwise to the first solution under vigorous stirring at room temperature over a period of 30 min. The subsequent steps were similar to those described above.

Synthesis of $\text{Li}_2\text{Zn}_3[\text{Fe}(\text{CN})_6]_2$: 2 g of $\text{K}_2\text{Zn}_3[\text{Fe}(\text{CN})_6]_2$ (1 eq.) was combined with 100 mL of DI water to obtain an aqueous suspension of the potassium electrolyte. The suspension was then heated to 80°C , after which 1.2 g of LiCl (10 eq.) was added. It was left at 80°C overnight for ion exchange. Subsequently, the supernatant was removed, and the obtained powder was washed three times using DI water with a 1:5 wt. ratio of powder to water, followed by drying at the desired temperature, preferably at 90°C , under a dynamic vacuum.

Synthesis of Na₂Mn[Fe(CN)₆]: The cathode material was obtained by precipitation of a solution of 2 g of Na₄[Fe(CN)₆]·10H₂O (1 eq.) in 100 mL of DI water with dropwise addition of 1 g of Mn(C₂O₂H₃)₂·4H₂O (1 eq.) in 100 mL of DI water in the presence of 2.4 g of NaCl (10 eq.) under stirring at room temperature. The mixture was stirred overnight, after which the supernatant was removed. The resulting powder was washed three times with DI water by centrifugation and re-suspension, followed by drying under a dynamic vacuum at 120 °C.

Synthesis of Na₃Sn: The alloy was prepared by combining pieces of sodium and tin in a stoichiometric manner via consecutive pressing and folding. The obtained sheet-like material was then heated at 300 °C and ground to a fine powder for further use. The synthesis was performed under an inert atmosphere.

Synthesis of Na₃PS₄: The solid electrolyte was prepared via mechanochemical synthesis adapting the procedure reported by Nguyen et al. [29] To this end, stoichiometric amounts of Na₂S and P₂S₅ were added to a ZrO₂ jar, followed by milling for 30 min at 250 rpm and another 30 min at 500 rpm.

Electrochemical Testing: Anode composite 1 was prepared by blending 95 wt.% Na₃Sn with 5 wt.% Na-ZHF-90. Anode composite 2 was prepared by blending 30 wt.% Li₄Ti₅O₁₂ with both 65 wt.% Na₃PS₄ and 5 wt.% Super C65 carbon black. Cathode composite was prepared by mixing 90 wt.% Na₂Mn[Fe(CN)₆] with 10 wt.% multiwalled carbon nanotubes. Full cell type 1 was assembled using 25 mg of anode composite 1 and 15 mg of cathode composite. Full cell type 2 was assembled using 50 mg of anode composite 2 and 15 mg of cathode composite. For testing of symmetrical cell type 1, 25 mg of anode composite 1 was used in the preparation of both electrodes. For testing of symmetrical cell type 2, 15 mg of cathode composite was used in the preparation of both electrodes. In all cells, Na-ZHF-90 (150 mg) served as a separator. Cells with a cross-section area of 0.785 cm² were cycled under a constant uniaxial stack pressure of 81 MPa at 45 °C (see Table S1, Supporting Information, for details on the cycling conditions), with 1C being equivalent to 100 mA/gCAM.

Electrochemical Impedance Spectroscopy: For EIS on cold-pressed samples, 200 mg of solid electrolyte powder was compressed at 437 MPa for 3 min using a customized setup with stainless steel dies and a PEEK sleeve (10 mm diameter). A pressure of 125 MPa was maintained during the measurements. EIS data were acquired from 0.1 Hz to 7 MHz with a 20 mV voltage amplitude using an SP-200 potentiostat (BioLogic, Seyssinet-Pariset, France). Temperature-dependent impedance spectra were recorded between 25 and 65 °C after equilibration for at least 1 h. Spectra fitting was performed using an equivalent circuit model of type RQ-W, with R, Q, and W being resistance, constant phase element, and Warburg element, respectively. The conductivity was calculated from the R, and the activation energy was obtained by Arrhenius fitting of the temperature-dependent conductivity. Residual porosity has not been considered.

Powder X-ray Diffraction: The materials were studied by PXRD in 0.03 mm glass capillaries (Hilgenberg, Malsfeld, Germany) using a STADI P (STOE, Darmstadt, Germany) diffractometer equipped with a Mythen 1K detector (DECTRIS, Baden, Switzerland) in Debye–Scherrer geometry with monochromatic Mo-K_{α1} radiation ($\lambda = 0.7093 \text{ \AA}$, 50 kV, 40 mA). The datasets were analyzed using TOPAS Academic V7. Le Bail analysis was performed after background correction (Chebyshev polynomial with 10 terms). Specifically, lattice parameters, zero-shift, axial divergence, and crystallite size (Gaussian and Lorentzian contributions) were extracted.

Thermogravimetric Analysis-Mass Spectrometry: TGA-MS was carried out using a SETARAM (Caluire-et-Cuire, France) thermal analyzer (SENSYS evo TG-DSC) equipped with a Pfeiffer (Asslar, Germany) OmniStar mass spectrometer. The measurement was conducted from room temperature to 500 °C under argon flow with a heating rate of 1 °C/min.

Inductively Coupled Plasma-Optical Emission Spectroscopy: ICP-OES was carried out using a Thermo Fisher Scientific (Waltham, MA, USA) iCAP 7600 DUO. The samples were

dissolved by acid digestion in a graphite furnace, and the elemental composition was probed using four different calibration solutions and two/three wavelengths per element.

Scanning Electron Microscopy: Morphological investigation by SEM was carried out on a LEO-1530 microscope (Carl Zeiss AG, Oberkochen, Germany).

3. Results

3.1. Structural Characterization

Open framework ZHF materials with targeted compositions of $\text{Li}_2\text{Zn}_3[\text{Fe}(\text{CN})_6]_2$, $\text{Na}_2\text{Zn}_3[\text{Fe}(\text{CN})_6]_2$, and $\text{K}_2\text{Zn}_3[\text{Fe}(\text{CN})_6]_2$, referred to as Li-ZHF, Na-ZHF, and K-ZHF, respectively, in the following, were synthesized by an aqueous, solution-based process. The sodium and potassium compounds were obtained by precipitation using either $\text{Na}_4[\text{Fe}(\text{CN})_6] \cdot 10\text{H}_2\text{O}$ or $\text{K}_4[\text{Fe}(\text{CN})_6] \cdot 10\text{H}_2\text{O}$ and nitrate salt as a zinc source in the presence of excess NaCl or KCl . The synthesis of the lithium compound was attempted by aqueous ion exchange from K-ZHF using excess LiCl at 80°C (details in the Materials and Methods Section).

The obtained materials were examined first by powder X-ray diffraction (PXRD). The respective data are shown in Figure 1a. Evidently, all materials produced similar diffraction patterns, and Le Bail analysis (see Table S2 and Figure S1, Supporting Information) revealed the presence of single-phase, garnet-type materials crystallizing in the $R\text{-}3c$ space group, in agreement with literature reports [30,31]. Schematic representations of the crystal structure are provided in Figure 1b,c. As can be seen, each $\text{Fe}(\text{CN})_6$ octahedron is coordinated by six zinc atoms, which in turn coordinate to the $\text{Fe}(\text{CN})_6$ octahedra themselves. The resulting six intercalation positions in the voids are partially occupied [26] by alkaline ions to yield in total one species per void to maintain charge neutrality. Additionally, it can be assumed that the PBA structure contains adsorbed (surface), interstitial (zeolitic), and coordinated (chemically bonded) water molecules, depending on the synthesis conditions [32].

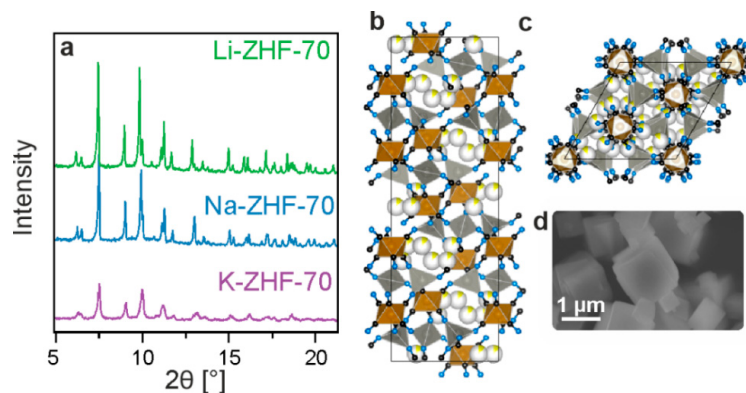


Figure 1. (a) PXRD patterns of the different ZHFs dried at 70°C . (b,c) Schematic representations of the garnet-type structure, with iron and zinc shown as brown and gray polyhedra, and carbon, nitrogen, and $\text{Li}^+/\text{Na}^+/\text{K}^+$ as black, blue, and yellow spheres, respectively. Note that the alkali-metal sites are only partially occupied. (d) SEM image collected from the Na-ZHF-70 sample.

Na-ZHF was further probed using scanning electron microscopy (SEM), indicating cuboid particles of about $1\text{ }\mu\text{m}$ in size, as shown in Figures 1d and S2 (Supporting Information). The different samples were also investigated by inductively coupled plasma-optical emission spectroscopy (ICP-OES), revealing Zn:Fe molar ratios of 1.58 ± 0.11 (Li-ZHF), 1.54 ± 0.05 (Na-ZHF), and 1.49 ± 0.08 (K-ZHF) (see Table S2, Supporting Information), corroborating the formation of trigonal structures rather than cubic $\text{Zn}_2[\text{Fe}(\text{CN})_6]$. Taken together, the results confirm the successful preparation of garnet-type ZHFs for all three alkaline ions.

During sample preparation, it was noticed that the drying temperature was affecting the lattice parameters of the ZHF samples. For systematic investigation into this effect, the

materials were dried at 70, 90, and 120 °C under a dynamic vacuum. The results from Le Bail fitting of the PXRD data collected from the different ZHFs are given in Tables 1 and S2 (Supporting Information).

Table 1. Overview of synthesized ZHFs, refinement results, and corresponding room-temperature ionic conductivities.

Sample	Assumed Stoichiometry	Drying Temperature [°C]	Unit-Cell Volume [nm ³]	Conductivity [mS/cm]
Li-ZHF-70	Li ₂ Zn ₃ [Fe(CN) ₆] ₂	70	4.434(2)	0.022
Li-ZHF-90	Li ₂ Zn ₃ [Fe(CN) ₆] ₂	90	4.422(2)	0.013
Li-ZHF-120	Li ₂ Zn ₃ [Fe(CN) ₆] ₂	120	4.459(6)	0.00034
Na-ZHF-70	Na ₂ Zn ₃ [Fe(CN) ₆] ₂	70	4.376(2)	0.031
Na-ZHF-90	Na ₂ Zn ₃ [Fe(CN) ₆] ₂	90	4.332(2)	0.17
Na-ZHF-120	Na ₂ Zn ₃ [Fe(CN) ₆] ₂	120	4.445(1)	0.21
K-ZHF-70	K ₂ Zn ₃ [Fe(CN) ₆] ₂	70	4.425(2)	0.092
K-ZHF-90	K ₂ Zn ₃ [Fe(CN) ₆] ₂	90	4.292(2)	0.015
K-ZHF-120	K ₂ Zn ₃ [Fe(CN) ₆] ₂	120	4.364(4)	0.0063

The unit-cell volumes of the Li-ZHFs are the largest overall (see Figure 2a). The Na- and K-ZHF samples exhibit slightly lower volumes, which vary strongly with drying temperature. In fact, all materials feature their lowest unit-cell volume at 90 °C. Increasing the drying temperature to 150 °C led to the formation of impurity phases, as determined by PXRD, indicating degradation (see Figure S3, Supporting Information). A previous study reported a decrease in unit-cell volume with freeze-drying of ZHFs [33]. Specifically, smaller coordinated alkaline ions led to more contraction of the unit cell during drying. Yet, the smallest ion considered was Na⁺. The observed shrinkage was more pronounced in samples having a relatively higher interstitial water content, i.e., for ZHFs containing the smaller alkaline ions. However, the findings cannot be directly compared with our observations, since the post-treatment, as well as the initial drying of materials (at 70 °C overnight), was different, which is also evident from the fact that freeze drying changes the space group in which the Na₂Zn₃[Fe(CN)₆]₂ crystallizes from R-3c to P2/c [33]. Nevertheless, more or less water may be present depending on the size of the coordinated alkaline ions. For example, in the related PBAs, the introduction of larger Ba²⁺ ions [$r(\text{Ba}^{2+}) \approx r(\text{Na}^+)$] has been shown to effectively prevent zeolitic water incorporation, which can be considered an intrinsic defect in PBA materials [34]. Similarly, here, one could expect less water coordination with the larger Na⁺ and K⁺ ions, which may explain their smaller (initial) unit-cell volumes. Similar trends have also been observed when comparing K-ZHF to Na-ZHF [33]. On the other hand, the synthesis method (ion exchange) to produce Li-ZHF required higher temperatures, which could account, at least to some degree, for the relative increase in volume.

To gain a better understanding of the drying process at elevated temperatures, thermogravimetric analysis coupled with mass spectrometry (TGA-MS) was applied to the samples initially dried at 70 °C (referred to as ZHF-70). The data shown in Figure 2b indicate that all materials lose weight upon heating, with an onset temperature of ~60 °C. For K-ZHF-70, after a mass loss of about 5.1 wt.%, a first plateau is reached at ~150 °C. The initial loss is primarily related to the release of interstitial water from the material, as evident from the measured ion current (see Figure 2c). The latter provides evidence for water release between 50 and 180 °C, but no such release beyond 200 °C. With increasing temperature, a second mass loss (by 6.2 wt.%) starting around 275 °C is noticed, corresponding to thermal degradation. This finding highlights the distinct difference to PBA cathodes, where a release of adsorbed water is observed until ~120 °C, and zeolitic water release only occurs at temperatures above 200 °C [27]. The mass loss of K-ZHF-70 up to

~ 150 °C corresponds roughly to that of two water molecules per sum formula. However, it should be noted that the materials were heated in an inert atmosphere rather than under a dynamic vacuum during this kind of measurement. The application of vacuum in the drying process is presumably more effective at low temperatures than what is indicated by TGA-MS. For the other two materials, Li-ZHF-70 and Na-ZHF-70, a gradual mass loss up to 225–250 °C is observed, after which no major losses are detected anymore. Therefore, the drying and decomposition processes likely overlap in these samples, with K-ZHF being more stable toward thermal degradation. Indeed, the ion currents measured by MS indicate continuous water release for the Li- and Na-ZHFs, with an apparent maximum at ~ 210 °C. In contrast, for K-ZHF, the highest release rate is found at ~ 120 °C. However, the increased ion flux in the Li- and Na-containing samples may also result from degradation, which occurs at 150 °C already. One could envision fracturing of the decomposing ZHF crystals, allowing for increased drying rates and leading to higher ion currents.

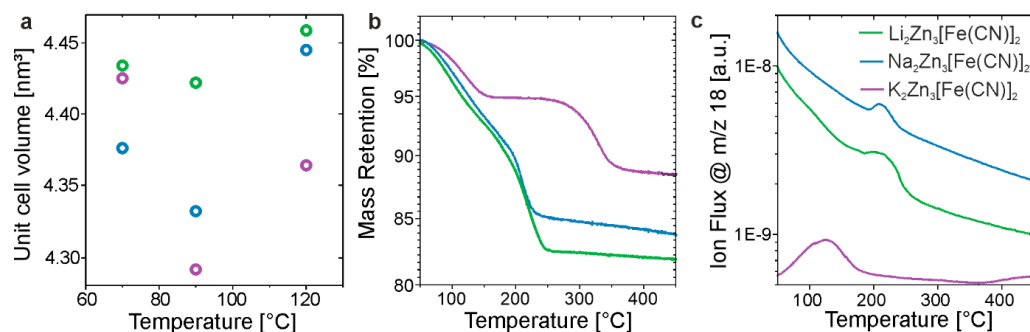


Figure 2. (a) Unit-cell volumes of the different ZHFs dried at temperatures ranging from 70 to 120 °C (Li-ZHF: green, Na-ZHF: blue, K-ZHF: purple). (b) TGA of the ZHF-70 samples and (c) corresponding ion currents related to water release from coupled MS measurements.

Overall, the TGA-MS results demonstrate a gradual release of interstitial water until ~ 250 °C for both the Na- and Li-ZHF-70. If the mass loss up to 150 °C (the plateau region in K-ZHF-70) is considered to only correspond to zeolitic water, the Na- and Li-ZHF-70 release ~ 2.7 and ~ 3.1 water molecules per sum formula, respectively. However, the amount of zeolitic water cannot be determined unambiguously from these experiments due to the convolution of degradation and drying. Also, it is important to mention that the data can be somewhat affected by the background signal (considering the measuring device and its environment). Yet, K-ZHF released the least water and is seemingly the most stable material, which agrees with the above hypothesis that the larger size of potassium ions leads to a lower fraction of incorporated water molecules.

3.2. Ionic Conductivity

To gain insight into the superionic conduction in the ZHF samples, electrochemical impedance spectroscopy (EIS) measurements were conducted on cold-pressed pellets. Interestingly, the materials are found to form stable pellets at very low compacting pressures, indicating good processability for solid-state batteries. The stability of the garnet-type framework upon densification was confirmed by PXRD before and after compacting the Na-ZHF-90 at 437 MPa (see Figure S3, Supporting Information). For conductivity measurements, about 200 mg of the powders were pressed at a uniaxial pressure of 125 MPa, after which the electrochemical impedance under ion-blocking conditions was recorded (details in the Materials and Methods Section). The respective room-temperature ionic conductivities are shown in Figure 3a and further given in Table 1.

The Na-ZHF samples dried at temperatures ≥ 90 °C exhibited the overall highest conductivities with $\sigma_{\text{ion},\text{rt}} \approx 0.2$ mS/cm, while Li-ZHF showed the lowest ranging from 0.00034 to 0.022 mS/cm. For all ZHFs, a strong dependence of conductivity on the drying conditions is found. For the K- and Li-ZHFs, a decrease in $\sigma_{\text{ion},\text{rt}}$ with increasing drying

temperature is noticed, while Na-ZHF shows the opposite trend. Explaining these trends is not trivial because various structure–property relations have been suggested for related PBA materials, intricately linking lattice size to ionic conductivity. For example, larger lattice parameters are reported to be beneficial to ion diffusion. Pasta and coworkers proposed that the ratio of ionic radius to lattice size may be used as a rule of thumb to assess conductivity [35,36]. Mechanistically, the positively charged (mobile) ions will be attracted to the negatively charged cyanide ligands, leading to an off-centered position in the thermodynamic ground state. Smaller alkaline ions coordinate closer to the cyanide ligands, while larger ones are located closer to the pore center [37]. In this model, a ladder mechanism of diffusion is considered, which determines the jump from one cyanide ligand to the next as the rate-limiting step (facilitated by larger cations). The mechanism predicts that TM-site vacancies negatively affect ionic conductivity, as they disturb the diffusion paths. For Rb^+ and Cs^+ , the opposite is observed experimentally though, meaning very large alkaline ions diffuse more readily in defective structures [38]. Diffusion of large ions in a lattice without TM vacancies is associated with a larger energy barrier due to a mismatch between ion size and free volume for diffusion [37]. This may be understood as a shift from the ladder mechanism, where the mobile ion is mostly coordinated to a single cyanide ligand, to a mechanism in which the ions jump from the center of the void to a neighboring center. The off-center displacement is also observed experimentally in ZHFs [33]. Upon freeze drying, the mobile ions coordinate closer to the elliptical window at the N terminal of the cyanide ligands. For ion diffusion in ZHFs, one could therefore also envision a ladder-like mechanism, with the rate-determining step being the movement from one window to the next through the pore volume.

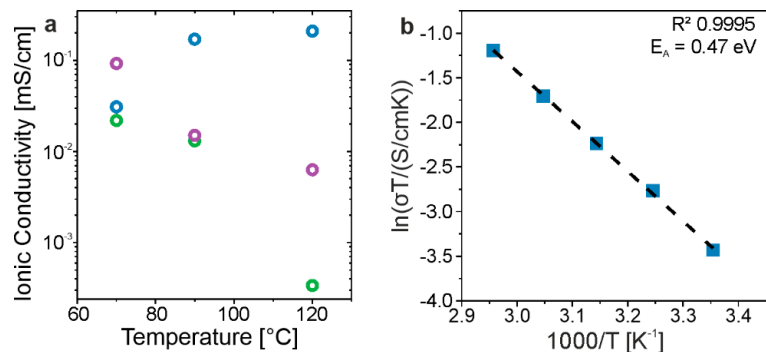


Figure 3. (a) Room-temperature ionic conductivities of the different ZHFs dried at temperatures ranging from 70 to 120 °C (Li-ZHF: green, Na-ZHF: blue, K-ZHF: purple). (b) Arrhenius plot of the temperature-dependent conductivity from EIS measurements conducted on the Na-ZHF-90 sample.

Moreover, the diffusion coefficient of sodium in $\text{Na}_2\text{Zn}_3[\text{Fe}(\text{CN})_6]_2$ has been reported as a function of the state of charge, or in other words, sodium content [32]. Specifically, the authors of that study established a connection between drying and improved diffusion coefficient and cycling performance. Interestingly, a rough estimation of ionic conductivity from the reported diffusion coefficient resulted in a value of 0.77 mS/cm (see Supporting Information for details), which is in reasonable agreement with our data considering the error from comparing electrode to bulk-diffusion measurements. Nevertheless, the precise diffusion mechanism in ZHFs remains largely unexplored, calling for density functional theory (DFT) calculations. For Na-ZHF-90, the activation energy for ion conduction was determined by temperature-dependent EIS measurements in the range between 25 and 65 °C. The results are presented in Figure 3b, and the corresponding Nyquist plots of the electrochemical impedance are shown in Figure S4 (Supporting Information). As expected, the conductivity follows an Arrhenius-type behavior. The activation energy was determined to be $E_A = 0.47 \text{ eV}$, similar to the best-performing PBA electrolyte (0.48 eV) [18]. Interestingly, the ionic conductivity of Na-ZHF-90 is significantly (2–20 fold) higher than

that of reported PBAs [18], which points toward fine differences in charge transport between the two material classes.

3.3. Electrochemical Testing

Na-ZHF-90 was also tested as an electrolyte, specifically as a separator, in pellet-stack solid-state sodium-ion batteries, with Na_3Sn and $\text{Na}_2\text{Mn}[\text{Fe}(\text{CN})_6]$ (Mn-PBA) (see the Materials and Methods Section for details on the synthesis) serving as anode and cathode, respectively. Full cells (type 1) were assembled and cycled as outlined in the Materials and Methods Section, as well as in Table S1 (Supporting Information). The voltage–capacity curves for some of the initial cycles at different current rates are shown in Figure 4a. With this kind of cell configuration, specific charge and discharge capacities of $q_{\text{ch}} = 103 \text{ mAh/g}_{\text{CAM}}$ and $q_{\text{dis}} = 62 \text{ mAh/g}_{\text{CAM}}$ were achieved at C/20 (with $1\text{C} = 100 \text{ mA/g}_{\text{CAM}}$), much lower than those reported in the literature for Mn-PBA in liquid-electrolyte-based cells [27]. Yet, the data demonstrate that a working full cell was successfully assembled. Charging and discharging at higher current rates led to lower capacities and larger overpotentials, along with severe voltage drops and interruptions. The latter features are not limited to the end of charge, where dendrite formation at the anode side may occur [39–42], but are rather arbitrarily distributed over both charge and discharge. Therefore, they are most likely related to the formation of resistive interfaces (between the different cell components) and interphases, resulting in sudden voltage changes due to (electro)chemical reactions.

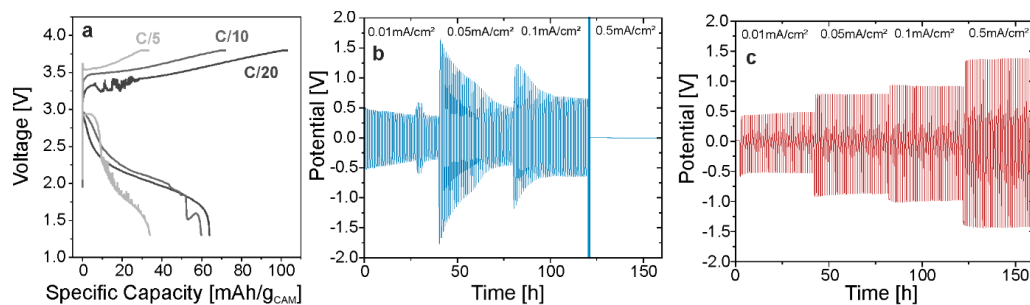


Figure 4. (a) Voltage profiles of full cell type 1 ($\text{Na}_3\text{Sn} \mid \text{Na-ZHF-90} \mid \text{Na}_2\text{Mn}[\text{Fe}(\text{CN})_6]$) at different rates of C/20, C/10, and C/5. The 1st, 3rd, and 5th cycles are shown. Cycling of symmetrical cells using (b) anode composite and (c) cathode composite.

To pin down the origin of the interface resistance (impedance growth), symmetrical cells of type electrode | Na-ZHF-90 | electrode were built and cycled at current densities ranging from 0.01 to 0.5 mA/cm^2 . The respective potential traces of cells using either anode or cathode composite are shown in Figure 4b,c (see Table S1, Supporting Information, for details on the cycling conditions). For the symmetrical cells with Na_3Sn electrodes, an overall increase in overpotential with increasing current density was observed. Moreover, cycling at 0.5 mA/cm^2 induced overpotentials exceeding 5 V, causing termination of the experiment. Notably, there was a sharp increase in overpotential with increasing current density, which however declined upon further cycling. This might be associated with the redox activity of certain decomposition species. Cycling of the symmetrical cells with Mn-PBA electrodes revealed a gradual increase in overpotential with increasing current density, from 0.5 V at 0.01 mA/cm^2 to 1.3 V at 0.5 mA/cm^2 , indicating that no severe side reactions between Na-ZHF-90 and Mn-PBA occur and further pointing toward the formation of “stable” interfaces. These results indicate that the solid electrolyte employed in this work exhibits an intrinsically poor reductive stability, leading to electrochemical decomposition in contact with Na_3Sn .

To validate this hypothesis, a second set of full cells (type 2) was assembled, in which an anode composite containing $\text{Li}_4\text{Ti}_5\text{O}_{12}$ (LTO), Na_3PS_4 , and Super C65 carbon black was utilized [43]. The higher redox potential of LTO vs. Na^+/Na compared to that of Na_3Sn should help minimize the electrochemical degradation of Na-ZHF-90. Voltage profiles

and cell capacities at current rates of C/20, C/10, and C/5 are presented in Figure 5a,b. Initially, the voltage window was set to 0.5–3.0 V, resulting in first-cycle specific capacities of $q_{\text{ch}} = 182 \text{ mAh/g}_{\text{CAM}}$ and $q_{\text{dis}} = 128 \text{ mAh/g}_{\text{CAM}}$ at C/20 (see Figure 5a). This corresponds to a relatively low initial Coulomb efficiency of 70%, due to irreversible side reactions occurring during cycling. Therefore, the upper cutoff voltage was lowered to 2.75 V in the subsequent cycles, as shown in Figure 5b. As expected, lower specific capacities of $q_{\text{dis}} = 79$ and 50 mAh/g_{CAM} were achieved at C/10 and C/5, respectively, in this case (see Figure 5b). Long-term cycling at C/5 revealed a capacity retention of 63% after 120 cycles (see Figure 5c). The full cells also exhibited a much lower overpotential than the type 1 design with Na₃Sn anode. This further stresses that the anode composite is primarily responsible for the poor cycling performance of the latter cells (type 1) and further confirms the limited cathodic stability of garnet-type ZHF solid electrolytes. Nevertheless, the results demonstrate that ZHF frameworks show promise for application in solid-state batteries.

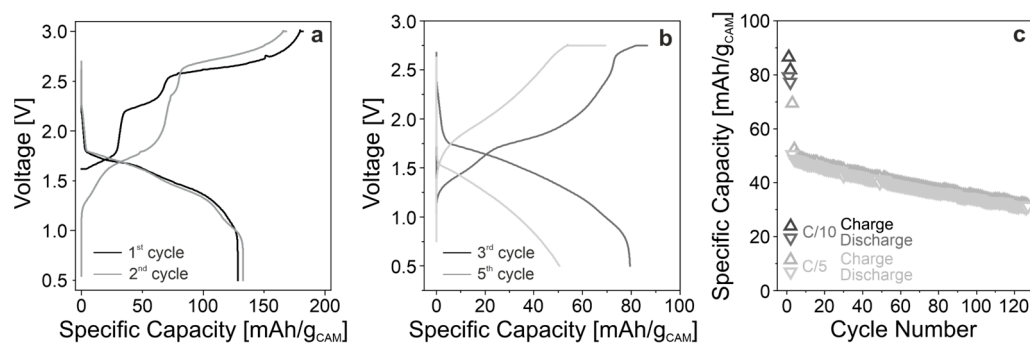


Figure 5. (a,b) Voltage profiles of full cell type 2 (LTO/Na₃PS₄/Super C65|Na-ZHF-90|Na₂Mn[Fe(CN)₆]) at different rates of C/20 (1st and 2nd cycles), C/10 (3rd cycle), and C/5 (5th cycle). Note that after the first two cycles, the voltage window was narrowed from 0.5–3.0 V to 0.5–2.75 V. (c) Long-term cycling at C/5 in the voltage window of 0.5–2.75 V.

4. Discussion

In this study, garnet-type zinc hexacyanoferrate frameworks were successfully produced (for the first time) by aqueous synthesis for use as electrolytes in solid-state batteries. Specifically, lithium, sodium, and potassium ion conductors were prepared and then compared with regard to drying behavior and room-temperature ionic conductivity. From this comparison, sodium zinc hexacyanoferrate emerged as the most promising solid electrolyte, exhibiting a significantly higher conductivity than previously reported Prussian blue analogues. Note that they offer higher conductivities as solid electrolytes by changing the ion-diffusion (channel) structure from cubic to garnet type. Overall, these materials offer ample opportunities for further investigation. In particular, the vacancy concentration, particle size, charge-carrier density (fraction of mobile ions), and composition represent intriguing possibilities for tailoring the transport properties as well as the electrochemical stability.

The application of sodium zinc hexacyanoferrate in solid-state sodium-ion batteries was also examined, and the cathodic stability was identified as being the most limiting factor. In conclusion, this work expands on the usage of Prussian blue-like compounds, which are usually of low cost, air-stable, easy to synthesize, and can be readily processed at low temperatures.

5. Patents

The authors declare the following competing interest(s): A patent was filed for some of this work through BASF SE and the Karlsruher Institut für Technologie (KIT).

Supplementary Materials: The following supporting information can be downloaded at: <https://www.mdpi.com/article/10.3390/batteries10100365/s1>, Table S1. Cell configurations and cycling conditions; Table S2. Results from Le Bail and ICP-OES analyses; Figure S1. PXRD pattern of Na-ZHF-90 and corresponding Le Bail fit. Measured, calculated, and difference data are shown in gray, red, and blue, respectively; Figure S2. SEM images at different magnifications of Na-ZHF-70; Figure S3. PXRD patterns of Na-ZHF-150 and Na-ZHF-90 (before and after compression); Figure S4. Nyquist plots of the electrochemical impedance of Na-ZHF-90 at temperatures ranging from 25 to 65 °C.

Author Contributions: Conceptualization, L.K., S.M., A.K. and F.S.; Formal analysis, L.K. and S.M.; Investigation, L.K., S.M., L.W. and Z.Z.-K.; Supervision, A.K., F.S. and T.B.; Writing—original draft, L.K.; Writing—review and editing, S.M., L.W., Z.Z.-K., A.K., F.S. and T.B. All authors have read and agreed to the published version of the manuscript.

Funding: This work was supported by the BASF SE. J.L. acknowledges the Fonds der Chemischen Industrie (FCI) for financial support. F.S. is grateful to the German Federal Ministry of Education and Research (BMBF) for funding within the project MELLi (03XP0447).

Data Availability Statement: The original contributions presented in the study are included in the article/Supplementary Material, further inquiries can be directed to the corresponding authors.

Acknowledgments: Thomas Bergfeldt and team (IAM-AWP, KIT) are acknowledged for performing the ICP-OES measurements. The authors would also like to thank Ruizhuo Zhang for SEM analysis.

Conflicts of Interest: Author Aleksandr Kondrakov is employed by the BASF SE. The remaining authors declare that the research was conducted in the absence of any commercial or financial relationships that could be construed as a potential conflict of interest.

References

1. Zhou, W.; Li, Y.; Xin, S.; Goodenough, J.B. Rechargeable Sodium All-Solid-State Battery. *ACS Cent. Sci.* **2017**, *3*, 52–57. [[CrossRef](#)] [[PubMed](#)]
2. Zhao, C.; Liu, L.; Qi, X.; Lu, Y.; Wu, F.; Zhao, J.; Yu, Y.; Hu, Y.-S.; Chen, L. Solid-State Sodium Batteries. *Adv. Energy Mater.* **2018**, *8*, 1703012. [[CrossRef](#)]
3. Ma, Q.; Liu, J.; Qi, X.; Rong, X.; Shao, Y.; Feng, W.; Nie, J.; Hu, Y.-S.; Li, H.; Huang, X.; et al. A new Na[(FSO₂)(n-C₄F₉SO₂)N]-based polymerelectrolyte for solid-state sodium batteries. *J. Mater. Chem. A* **2017**, *5*, 7738–7743. [[CrossRef](#)]
4. Ma, Q.; Hu, Y.; Li, H.; Chen, L.; Huang, X.; Zhou, Z. An sodium bis(trifluoromethanesulfonyl)imide-based polymer electrolyte for solid-state sodium batteries. *Acta Phys. Chim. Sin.* **2018**, *34*, 213–218.
5. Moreno, J.S.; Armand, M.; Berman, M.B.; Greenbaum, S.G.; Scrosati, B.; Panero, S. Composite PEOn:NaTFSI polymer electrolyte: Preparation, thermal and electrochemical characterization. *J. Power Sources* **2014**, *248*, 695–702. [[CrossRef](#)]
6. Song, S.; Kotobuki, M.; Zheng, F.; Xu, C.; Savilov, S.V.; Hu, N.; Lu, L.; Wang, Y.; Li, W.D.Z. A hybrid polymer/oxide/ionic-liquid solid electrolyte for Na-metal batteries. *J. Mater. Chem. A* **2017**, *5*, 6424–6431. [[CrossRef](#)]
7. Goodwin, L.E.; Till, P.; Bhardwaj, M.; Nazer, N.; Adelhelm, P.; Tietz, F.; Zeier, W.G.; Richter, F.H.; Janek, J. Protective NaSICON Interlayer between a Sodium–Tin Alloy Anode and Sulfide-Based Solid Electrolytes for All-Solid-State Sodium Batteries. *ACS Appl. Mater. Interfaces* **2023**, *15*, 50457–50468. [[CrossRef](#)]
8. Wu, J.-F.; Wang, Q.; Guo, X. Sodium-ion conduction in Na₂Zn₂TeO₆ solid electrolytes. *J. Power Sources* **2018**, *402*, 513–518. [[CrossRef](#)]
9. Yang, Z.; Tang, B.; Xie, Z.; Zhou, Z. NASICON-Type Na₃Zr₂Si₂PO₁₂ Solid-State Electrolytes for Sodium Batteries. *ChemElectroChem* **2021**, *8*, 1035–1047. [[CrossRef](#)]
10. Yu Yao, Y.-F.; Kummer, J.T. Ion exchange properties of and rates of ionic diffusion in beta-alumina. *J. Inorg. Nucl. Chem.* **1967**, *29*, 2453–2475. [[CrossRef](#)]
11. Wu, E.A.; Banerjee, S.; Tang, H.; Richardson, P.M.; Doux, J.M.; Qi, J.; Zhu, Z.; Grenier, A.; Li, Y.; Zhao, E.; et al. A stable cathode-solid electrolyte composite for high-voltage, long-cycle-life solid-state sodium-ion batteries. *Nat. Commun.* **2021**, *12*, 1256. [[CrossRef](#)] [[PubMed](#)]
12. Schlem, R.; Banik, A.; Eckhardt, M.; Zobel, M.; Zeier, W.G. Na_{3-x}Er_{1-x}Zr_xCl₆—A Halide-Based Fast Sodium-Ion Conductor with Vacancy-Driven Ionic Transport. *ACS Appl. Energy Mater.* **2020**, *3*, 10164–10173. [[CrossRef](#)]
13. Kwak, H.; Lyoo, J.; Park, J.; Han, Y.; Asakura, R.; Remhof, A.; Battaglia, C.; Kim, H.; Hong, S.T.; Jung, Y.S. Na₂ZrCl₆ enabling highly stable 3 V all-solid-state Na-ion batteries. *Energy Storage Mater.* **2021**, *37*, 47–54. [[CrossRef](#)]
14. Tsuji, F.; Nasu, A.; Sakuda, A.; Tatsumisago, M.; Hayashi, A. Mechanochemical synthesis and characterization of Na_{3-x}P_{1-x}W_xS₄ solid electrolytes. *J. Power Sources* **2021**, *506*, 230100. [[CrossRef](#)]

15. Hayashi, A.; Noi, K.; Sakuda, A.; Tatsumisago, M. Superionic glass-ceramic electrolytes for room-temperature rechargeable sodium batteries. *Nat. Commun.* **2012**, *3*, 856. [[CrossRef](#)]
16. Banerjee, A.; Park, K.H.; Heo, J.W.; Nam, Y.J.; Moon, C.K.; Oh, S.M.; Hong, S.-T.; Jung, Y.S. Na_3SbS_4 : A Solution Processable Sodium Superionic Conductor for All-Solid-State Sodium-Ion Batteries. *Angew. Chem. Int. Ed.* **2016**, *55*, 9634–9638. [[CrossRef](#)]
17. Kim, T.W.; Park, K.H.; Choi, Y.E.; Lee, J.Y.; Jung, Y.S. Aqueous-solution synthesis of Na_3SbS_4 solid electrolytes for all-solid-state Na-ion batteries. *J. Mater. Chem. A* **2018**, *6*, 840–844. [[CrossRef](#)]
18. Kim, T.; Hyeok Ahn, S.; Song, Y.Y.; Jin Park, B.; Lee, C.; Choi, A.; Kim, M.H.; Seo, D.H.; Jung, S.K.; Lee, H.W. Prussian Blue-Type Sodium-ion Conducting Solid Electrolytes for All Solid-State Batteries. *Angew. Chem. Int. Ed.* **2023**, *62*, e202309852. [[CrossRef](#)]
19. Pshinko, G.N.; Puzyrnaya, L.N.; Shunkov, V.S.; Kosorukov, A.A.; Demchenko, V.Y. Removal of Cesium and Strontium Radionuclides from Aqueous Media by Sorption onto Magnetic Potassium Zinc Hexacyanoferate(II). *Radiochemistry* **2016**, *58*, 491–497. [[CrossRef](#)]
20. Kawamura, S.; Kuraku, H.; Kurotaki, K. Adsorption characteristics of radionuclides on nickel hexacyanoferate(II). *Anal. Chim. Acta* **1970**, *81*, 91–97. [[CrossRef](#)]
21. Jassal, V.; Shanker, U.; Kaith, B.S.; Shankar, S. Green synthesis of potassium zinc hexacyanoferate nanocubes and their potential application in photocatalytic degradation of organic dyes. *RSC Adv.* **2015**, *5*, 26141–26149. [[CrossRef](#)]
22. Arida, H.A.; Aglan, R.F. A Solid-State Potassium Selective Electrode Based on Potassium Zinc Ferrocyanide Ion Exchanger. *Anal. Lett.* **2003**, *36*, 895–907. [[CrossRef](#)]
23. Oliver-Tolentino, M.A.; Vazquez-Samperio, J.; Cabrera-Sierra, R.; Reguera, E. Materials for aqueous sodium-ion batteries: Cation mobility in a zinc hexacyanoferate electrode. *RSC Adv.* **2016**, *6*, 108627–108634. [[CrossRef](#)]
24. He, B.; Man, P.; Zhang, Q.; Wang, C.; Zhou, Z.; Li, C.; Wei, L.; Yao, Y. Conversion Synthesis of Self-Standing Potassium Zinc Hexacyanoferate Arrays as Cathodes for High-Voltage Flexible Aqueous Rechargeable Sodium-Ion Batteries. *Small* **2019**, *15*, 1905115. [[CrossRef](#)] [[PubMed](#)]
25. Lee, H.; Il Kim, Y.; Park, J.K.; Choi, J.W. Sodium zinc hexacyanoferate with a well-defined open framework as a positive electrode for sodium ion batteries. *Chem. Commun.* **2012**, *48*, 8416–8418. [[CrossRef](#)]
26. Heo, J.W.; Chae, M.S.; Hyoung, J.; Hong, S.T. Rhombohedral Potassium-Zinc Hexacyanoferate as a Cathode Material for Nonaqueous Potassium-Ion Batteries. *Inorg. Chem.* **2019**, *58*, 3065–3072. [[CrossRef](#)]
27. Song, J.; Wang, L.; Lu, Y.; Liu, J.; Guo, B.; Xiao, P.; Lee, J.J.; Yang, X.Q.; Henkelman, G.; Goodenough, J.B. Removal of Interstitial H_2O in Hexacyanometallates for a Superior Cathode of a Sodium-Ion Battery. *J. Am. Chem. Soc.* **2015**, *137*, 2658–2664. [[CrossRef](#)]
28. Xiao, P.; Song, J.; Wang, L.; Goodenough, J.B.; Henkelman, G. Theoretical Study of the Structural Evolution of a $\text{Na}_2\text{FeMn}(\text{CN})_6$ Cathode upon Na Intercalation. *Chem. Mater.* **2015**, *27*, 3763–3768. [[CrossRef](#)]
29. Nguyen, H.; Banerjee, A.; Wang, X.; Tan, D.; Wu, E.A.; Doux, J.-M.; Stephens, R.; Verbist, G.; Meng, Y.S. Single-step synthesis of highly conductive Na_3PS_4 solid electrolyte for sodium all solid-state batteries. *J. Power Sources* **2019**, *435*, 126623. [[CrossRef](#)]
30. Siebert, H.; Jentsch, W. Rhomboedrisch kristallisierende Zink-hexacyanometallate(III) $\text{Zn}_3[\text{M}(\text{CN})_8]_2$. *Z. Naturforsch.* **1981**, *36b*, 123–124. [[CrossRef](#)]
31. Rodríguez-Hernández, J.; Reguera, E.; Lima, E.; Balmaseda, J.; Martínez-García, R.; Yee-Madeira, H. An atypical coordination in hexacyanometallates: Structure and properties of hexagonal zinc phases. *J. Phys. Chem. Solids* **2007**, *68*, 1630–1642. [[CrossRef](#)]
32. Oliver-Tolentino, M.; Ramos-Sánchez, G.; Guzmán, G.; Avila, M.; González, I.; Reguera, E. Water effect on sodium mobility in zinc hexacyanoferate during charge/discharge processes in sodium ion-based battery. *Solid State Ion.* **2017**, *312*, 67–72. [[CrossRef](#)]
33. Avila, M.; Rodríguez-Hernández, J.; Lemus-Santana, A.A.; Reguera, E. Cation mobility and structural changes on the water removal in zeolite-like zinc hexacyanometallates (II). *J. Phys. Chem. Solids* **2011**, *72*, 988–993. [[CrossRef](#)]
34. Liu, X.; Gong, H.; Han, C.; Cao, Y.; Li, Y.; Sun, J. Barium ions act as defenders to prevent water from entering prussian blue lattice for sodium-ion battery. *Energy Storage Mater.* **2023**, *57*, 118–124. [[CrossRef](#)]
35. Hurlbutt, K.; Wheeler, S.; Capone, I.; Pasta, M. Prussian Blue Analogs as Battery Materials. *Joule* **2018**, *2*, 1950–1960. [[CrossRef](#)]
36. Takachi, M.; Fukuzumi, Y.; Moritomo, Y. Na^+ diffusion kinetics in nanoporous metal-hexacyanoferates. *Dalt. Trans.* **2016**, *45*, 458–461. [[CrossRef](#)]
37. Nordstrand, J.; Toledo-Carrillo, E.; Kloof, L.; Dutta, J. Sodium to cesium ions: A general ladder mechanism of ion diffusion in prussian blue analogs. *Phys. Chem. Chem. Phys.* **2022**, *24*, 12374–12382. [[CrossRef](#)]
38. Moritomo, Y.; Igashira, K.; Kim, J.; Tanaka, H. Size Dependent Cation Channel in Nanoporous Prussian Blue Lattice. *Appl. Phys. Express* **2009**, *2*, 085001. [[CrossRef](#)]
39. Ning, Z.; Li, G.; Melvin, D.L.R.; Chen, Y.; Bu, J.; Spencer-Jolly, D.; Liu, J.; Hu, B.; Gao, X.; Perera, J.; et al. Dendrite initiation and propagation in lithium metal solid-state batteries. *Nature* **2023**, *618*, 287–293. [[CrossRef](#)]
40. Ma, Q.; Ortmann, T.; Yang, A.; Sebold, D.; Burkhardt, S.; Rohnke, M.; Tietz, F.; Fattakhova-Rohlfing, D.; Janek, J.; Guillou, O. Enhancing the Dendrite Tolerance of NaSICON Electrolytes by Suppressing Edge Growth of Na Electrode along Ceramic Surface. *Adv. Energy Mater.* **2022**, *12*, 2201680. [[CrossRef](#)]
41. Medenbach, L.; Bender, C.L.; Haas, R.; Mogwitz, B.; Pompe, C.; Adelhelm, P.; Schröder, D.; Janek, J. Origins of Dendrite Formation in Sodium–Oxygen Batteries and Possible Countermeasures. *Energy Technol.* **2017**, *5*, 2265–2274. [[CrossRef](#)]

42. Singh, D.K.; Henss, A.; Mogwitz, B.; Gautam, A.; Horn, J.; Krauskopf, T.; Burkhardt, S.; Sann, J.; Richter, F.H.; Janek, J. Li₆PS₅Cl microstructure and influence on dendrite growth in solid-state batteries with lithium metal anode. *Cell Rep. Phys. Sci.* **2022**, *3*, 101043. [[CrossRef](#)]
43. Sun, Y.; Zhao, L.; Pan, H.; Lu, X.; Gu, L.; Hu, Y.-S.; Li, H.; Armand, M.; Ikuhara, Y.; Chen, L.; et al. Direct atomic-scale confirmation of three-phase storage mechanism in Li₄Ti₅O₁₂ anodes for room-temperature sodium-ion batteries. *Nat. Commun.* **2013**, *4*, 1870. [[CrossRef](#)] [[PubMed](#)]

Disclaimer/Publisher’s Note: The statements, opinions and data contained in all publications are solely those of the individual author(s) and contributor(s) and not of MDPI and/or the editor(s). MDPI and/or the editor(s) disclaim responsibility for any injury to people or property resulting from any ideas, methods, instructions or products referred to in the content.